ACS Infectious Diseases

pubs.acs.org/journal/aidcbc

Article

Nipah Virus V Protein Binding Alters MDA5 Helicase Folding Dynamics

Nicole D. Wagner,[△] Hejun Liu,[△] Henry W. Rohrs, Gaya K. Amarasinghe, Michael L. Gross, and Daisy W. Leung*

Cite This: *ACS Infect. Dis.* 2022, 8, 118−128

Read Online

ACCESS | Metrics & More | Article Recommendations | Supporting Information

ABSTRACT: Nipah virus (NiV) is an emerging and deadly zoonotic paramyxovirus that is responsible for periodic epidemics of acute respiratory illness and encephalitis in humans. Previous studies have shown that the NiV V protein antagonizes host antiviral immunity, but the molecular mechanism is incompletely understood. To address this gap, we biochemically characterized NiV V binding to the host pattern recognition receptor MDA5. We find that the C-terminal domain of NiV V (V_{CTD}) is sufficient to bind the $MDA5_{SF2}$ domain when recombinantly co-expressed in bacteria. Analysis by hydrogen−deuterium exchange mass spectrometry (HDX-MS) studies revealed that NiV V_{CTD} is conformationally dynamic, and binding to MDA5 reduces the dynamics of V_{CTD}. Our results also suggest that the β-sheet region in between the MDA5 Hel1, Hel2, and Hel2i domains exhibits rapid HDX. Upon V_{CTD} binding, these β-sheet and adjacent residues show significant protection. Collectively, our findings suggest that NiV V binding disrupts the helicase fold and dynamics of MDA5 to antagonize host antiviral immunity.

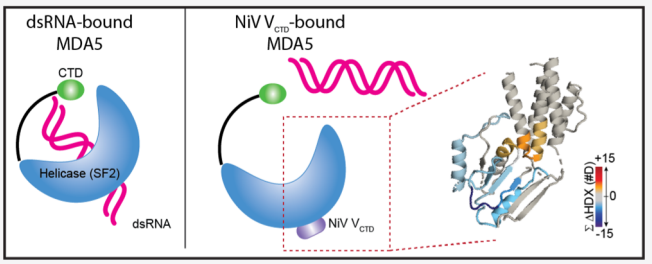

KEYWORDS: *Nipah virus, V protein, MDA5, IFN antagonist, hydrogen−deuterium exchange mass spectrometry*

Nipah virus (NiV) is an emerging zoonotic pathogen that causes severe respiratory disease and encephalitis associated with human fatalities.[1−5] NiV was first identified in Malaysia and Singapore as the source of an outbreak of disease among pigs and subsequently in humans.[6,7] Since then, recurring outbreaks have been documented in other parts of Asia, primarily in Bangladesh and India, with case fatality rates as high as 75%. Isolates from Malaysia and Bangladesh are genetically distinct. While there is high nucleotide homology (>91%) between the Malaysia and Bangladesh strains, the sequence heterogeneity in NiV genes or proteins may account for the differences in the transmission mode and rates.[8,9] Currently, there are no approved, effective prophylactics or therapeutics available for NiV infection.

NiV, along with Hendra virus (HeV), are henipaviruses within the paramyxovirus family of the nonsegmented, negative-strand RNA viruses. These also include parainfluenza virus 5 (PIV5), measles virus (MV), mumps virus (MuV), and Sendai virus (SeV).[10−13] The NiV genome encodes for four nonstructural proteins (P, V, W, and C) that are generated from the P gene and that function to inhibit host innate immune responses. V and W proteins are produced through RNA editing during transcription, and the C protein is expressed through leaky scanning and an alternative initiation codon site during ribosomal translation.[2,10,14−17] Thus, P, V, and W proteins share a common N-terminal domain (NTD), but each has distinct C-terminal domains (CTDs). NiV V_{CTD} also contains a conserved histidine and several cysteine residues, which likely form two zinc finger (ZnF) motifs based upon sequence homology to PIV5 and MV V_{CTD}s.[18−22]

Like other paramyxoviruses, NiV V proteins function as interferon (IFN) antagonists to inhibit host antiviral signaling. Earlier studies showed that the NiV V protein is a major determinant of pathogenesis.[23−25] Recombinant Nipah virus Malaysia with V protein knockout ($rNiV_M$-V^{KO}) is severely attenuated compared to WT virus or virus with W protein knockout due to reduced inhibition of the innate immune response; this allows for a potent neutralizing antibody response and viral clearance.[23] The lack of serious disease in animals infected with $rNiV_M$-V^{KO} points to the V protein having a prominent and early role in modulating immune responses and controlling disease progression. NiV V targets the host cytoplasmic pattern-recognition receptor (PRR) melanoma differentiation-associated protein 5 (MDA5) that detects viral RNAs and triggers IFN production and antiviral gene expression to control viral infections.[26−34] MDA5 contains a superfamily 2 (SF2) helicase domain preceded by

Received: July 30, 2021
Published: December 8, 2021

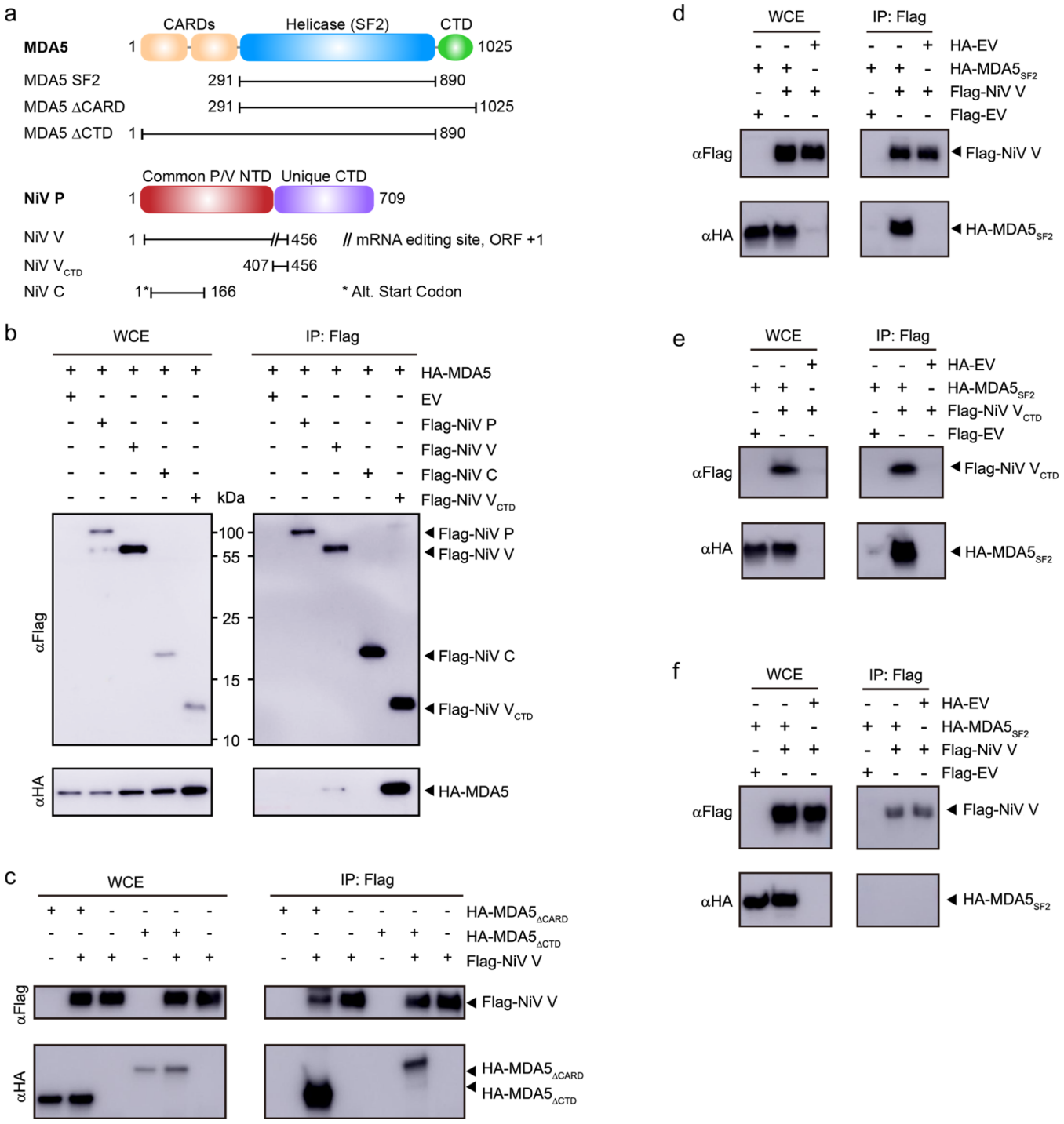

Figure 1. NiV V_{CTD} protein binds the $MDA5_{SF2}$ domain. (a) Domain architecture and constructs of NiV P/V/C and MDA5 proteins. (b) co-IP of NiV P gene-encoded proteins with MDA5. NiV P, V, C, V_{CTD}, or empty vector (EV) plasmids encoding a fusion N-terminal FLAG epitope tag were co-transfected with the human MDA5 or EV plasmid encoding a fusion N-terminal HA epitope tag. HEK293T cells were harvested at 48 h after co-transfection. Cells were lysed, and the resultant lysate was clarified as a whole cell extract (WCE). Anti-FLAG M2 beads were incubated with each WCE and washed before elution with the FLAG peptide for Western blot. (c) NiV V co-immunoprecipitates with MDA5 truncations. (d) NiV V co-immunoprecipitates with the $MDA5_{SF2}$ domain. (e) NiV V_{CTD} co-immunoprecipitates with the $MDA5_{SF2}$ domain. (f) NiV V cannot pull-down $MDA5_{SF2}$ when expressed separately, and lysates were mixed together prior to co-IP. Images show representative experimental data of three biological repeats.

two tandem N-terminal caspase activation and recruitment domains (CARDs) that are involved in autoregulatory activities and a CTD that binds double-stranded RNA (dsRNA). Previous studies showed that V proteins of several paramyxoviruses, including NiV, PIV5, HeV, SeV, and MuV, all bind MDA5 and not RIG-I.[33−35] In addition, NiV V targets the STAT1 transcription factor. NiV P/V_{NTD} binds to STAT1 and prevents its tyrosine phosphorylation and activation,[14,36−38] whereas NiV W_{CTD} contains a nuclear localization sequence that allows it to also sequester STAT1 in the nucleus

https://doi.org/10.1021/acsinfecdis.1c00403
ACS Infect. Dis. 2022, 8, 118−128

and prevent transcriptional activation of IFN-stimulated genes.[38−41] Although these studies show that NiV can target MDA5 and STAT1, how NiV proteins mediate these functions remains incompletely defined. Furthermore, the amino acid sequence encoded by NiV P/V/W_{NTD} is different from other paramyxovirus P proteins, suggesting that NiV may use a distinct mechanism to antagonize IFN responses.

Here, we employed a combined approach to validate and to characterize biochemically the interaction between NiV V and MDA5. Co-immunoprecipitation (co-IP) and *in vitro* pulldown assays demonstrated direct binding between NiV V and MDA5 proteins. Further analysis defined the regions NiV V_{CTD} and the MDA5 SF2 ($MDA5_{SF2}$) domain as sufficient for interactions. Hydrogen−deuterium exchange mass spectrometry (HDX-MS) on NiV V_{CTD} revealed a dynamic protein that becomes protected from HDX upon binding to the $MDA5_{SF2}$ domain. HDX-MS studies on $MDA5_{SF2}$ identified a highly dynamic β-sheet region that exposes a potential site for V_{CTD} binding. Additional HDX-MS studies on the NiV V_{CTD}/$MDA5_{SF2}$ complex suggest that NiV V_{CTD} binds to surfaces adjacent to this dynamic region within the SF2 domain. Altogether, our results support that NiV V binding disrupts the MDA5 fold and dynamics to antagonize host antiviral immunity.

RESULTS

NiV V_{CTD} Binds to $MDA5_{SF2}$. To further characterize the interaction between NiV V and MDA5, we first co-transfected plasmids encoding HA-tagged MDA5 and Flag-tagged P, V, or C proteins from the Malaysia strain (accession AAK50551) into HEK293T cells. We used the Malaysia strain sequence, since this was the first Nipah virus identified, even though the Bangladesh strain has been shown to be more pathogenic. Flag co-IP revealed that the NiV V protein immunoprecipitates with full-length MDA5 (Figures 1a,b and S1a), as shown previously.[18,33−35,42−47] Transfections with the NiV V CTD (V_{CTD}; encoding residues G407−G456) displayed stronger co-IP of full-length MDA5 relative to full-length V. Previous studies on full-length V revealed that the V protein alone is largely intrinsically disordered with some residual secondary structure and that regions in V can undergo a structural transition upon interactions with a binding partner.[48] Our results here raise the possibility that other regions in the full-length V protein may prevent the V_{CTD} from binding MDA5 through interactions with other host factors during co-IP that can restrict the conformation of V or the accessibility of the V_{CTD}. While this needs further testing, the isolated V_{CTD} is sufficient and strongly binds toMDA5, consistent with earlier observations.[33−35,43]

To define the minimal region in MDA5 that interacts with the NiV V_{CTD}, we generated a series of MDA5 truncations that were co-transfected with NiV V_{CTD} and subjected to co-IP studies. Our results indicate that both $MDA5_{\Delta CARD}$ (encoding residues 291−1025) and $MDA5_{\Delta CTD}$ (encoding residues 1−890) co-immunoprecipitates with NiV V, suggesting that the CARDs and the C-terminal RNA binding domain are not required for the NiV V interaction (Figures 1c and S1b). We next tested binding to the $MDA5_{SF2}$ domain (encoding residues 291−890) that contains the DECH helicase and pincer region. We found that $MDA5_{SF2}$ co-immunoprecipitates with both NiV V full length (Figures 1d and S1c) and to its isolated V_{CTD} (Figures 1e and S1c).

To further validate the interaction between NiV V_{CTD} and the $MDA5_{SF2}$ domain and to show direct binding, we next transfected the $MDA5_{SF2}$ and NiV V constructs into separate pools of HEK293T cells, mixed the WCEs together, and performed the co-IP. However, we found that NiV V does not co-IP with $MDA5_{SF2}$ under these conditions (Figures 1f and S1d). We next tested if recombinant maltose binding protein (MBP)-tagged NiV V_{CTD} and the $MDA5_{SF2}$ domain expressed separately in *Escherichia coli* bind in *in vitro* pulldown assays. When we mixed lysates containing each protein together prior to pulldown, we observed no binding (Figure 2a), consistent

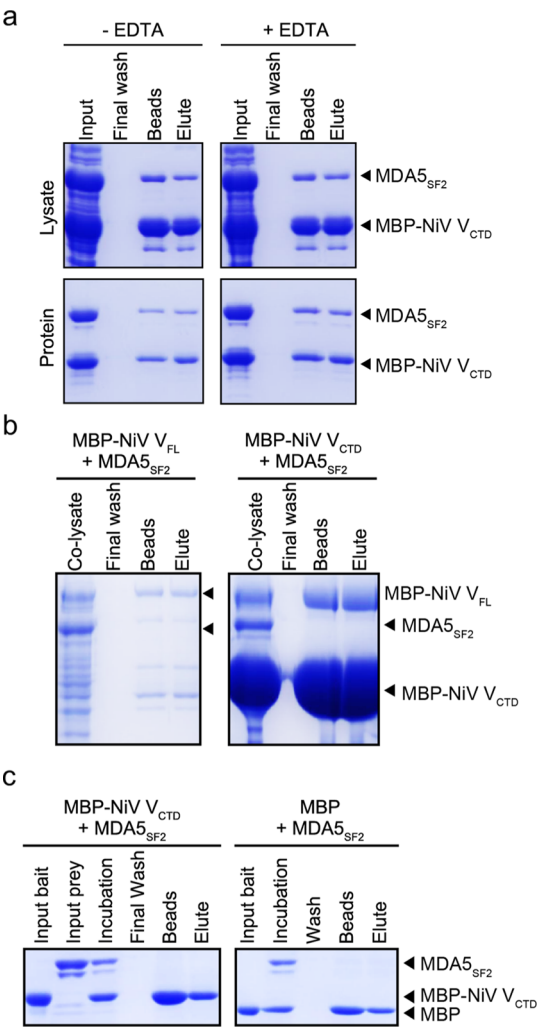

Figure 2. Co-expression of NiV V_{CTD} with $MDA5_{SF2}$ produces a soluble protein complex. (a) NiV V_{CTD} co-expressed with $MDA5_{SF2}$ showed direct interactions by *in vitro* pulldown assay. *E. coli* cells co-expressing both MBP−NiV V_{CTD} and $MDA5_{SF2}$ were lysed and clarified prior to a MBP pulldown assay on amylose resin in the absence (left) and presence (right) of 5 mM EDTA. (b) Co-lysis of bacterial cells containing NiV V_{CTD} and $MDA5_{SF2}$ that do not pull-down each other. *E. coli* cells expressing NiV V_{CTD} were mixed with cells expressing $MDA5_{SF2}$ prior to homogenization. The resultant supernatant after clarification of the co-lysates was applied to amylose resin and washed as in (a). (c) Individually purified NiV V_{CTD} in *E. coli* cells does not pull-down $MDA5_{SF2}$. Amylose beads were incubated with either the MBP tag alone or with the MBP−NiV V_{CTD} protein as bait mixed with a separately purified $MDA5_{SF2}$ domain as prey. After stringent washing, proteins bound on the resin were eluted with buffer containing 15 mM maltose.

https://doi.org/10.1021/acsinfecdis.1c00403
ACS Infect. Dis. 2022, 8, 118−128

with our observations in HEK293T cells. When we performed pulldown assays using individually purified proteins, we also observed no detectable binding (Figure 2b). Together, these results suggest that the interaction between NiV V_{CTD} and the $MDA5_{SF2}$ domain requires additional host factors that may be present during co-IP or requires co-translational assembly. We next tested co-expression of MBP−NiV V_{CTD} with the $MDA5_{SF2}$ domain in bacteria and found that MBP-tagged NiV V_{CTD} binds directly to the $MDA5_{SF2}$ domain by pulldown assay (Figure 2c, left panel), eliminating the possibility that other factors are involved. Because the NiV V_{CTD} contains highly conserved cysteine-rich domains that are predicted to form two Zn finger motifs,[20,21,49] analogous to that observed in the PIV5 crystal structures[18,50] (Figure S1e), we also performed *in vitro* pulldown assays in the presence of ethylenediaminetetraacetic acid (EDTA). We find that addition of EDTA had no impact on binding (Figure 2c, right panel), suggesting the formation of a stable complex. Together, our results indicate that simultaneous expression of the $MDA5_{SF2}$ domain with NiV V_{CTD} may be necessary for proper folding and stability.

$MDA5_{SF2}$ Can Modulate the Dynamics of the NiV V_{CTD}. Because the structures for NiV V or V_{CTD} are not currently known, we used HDX-MS to structurally characterize the NiV V_{CTD}. HDX-MS reports on changes in solvent accessibility or hydrogen bonding of backbone amide groups; thus, HDX is sensitive to protein dynamics, conformational changes, and binding sites.[51,52] Peptide digestion and bottom-up analysis of the isolated MBP-tagged NiV V_{CTD} produced 24 unique peptides, reporting on 84% of the construct (Figure S2a). The most N-terminal residue of every peptide is prone to fast back-exchange and thus is not considered in the interpretation.[53] More N-terminal residues show very low HDX at short incubation times (residues 405−434) (Figure 3a). The C-terminal end of V_{CTD} (residues 433−454) shows a high degree of HDX, even after short HDX incubation times, indicating a more disordered structure.

Analysis of the MBP−NiV V_{CTD}/$MDA5_{SF2}$ complex reveals that the N-terminus of NiV V_{CTD} is protected from HDX and throughout much of the V_{CTD} (Figure 3b). One region of the protein (represented by two peptides: 402−415 aa and 426−432 aa) indicate a static binding site (with slow on/off rates), where the HDX kinetic curves of the unbound (free state) and bound (in complex with $MDA5_{SF2}$) protein run in parallel (Figure 3b,c). The intervening region (415−416 aa and 417−425 aa) shows increased HDX for the bound state, suggesting that these peptides become less hydrogen-bonded or more exposed for the MBP−NiV V_{CTD}/$MDA5_{SF2}$ complex than in the unbound state; in fact, part of this region of V_{CTD} (residues 415−416) in the complex shows very high HDX after longer incubation times, consistent with little hydrogen bonding. In the region containing residues 433−445, the kinetic plots for unbound and bound converge with time, suggesting that the region becomes more dynamic and less bonded (faster off rate) than the more N-terminal binding regions. The C-terminal end of V_{CTD} (residues 445−456) shows little to no difference in HDX between bound and unbound. The V_{CTD} contains a histidine (H408) and seven cysteine (C415, C427, C431, C443, C445, C448, and C452) residues that are conserved in all paramyxovirus V_{CTD}s.[22,45] Parallels to PIV5 V proteins suggest that these residues are important for zinc coordination and formation of a Zn finger motif.[18,19] The data shown here reveal that H408, C415, C448, and C452, which form the larger first Zn finger, undergo less changes in HDX upon $MDA5_{SF2}$ binding compared to the four central cysteine

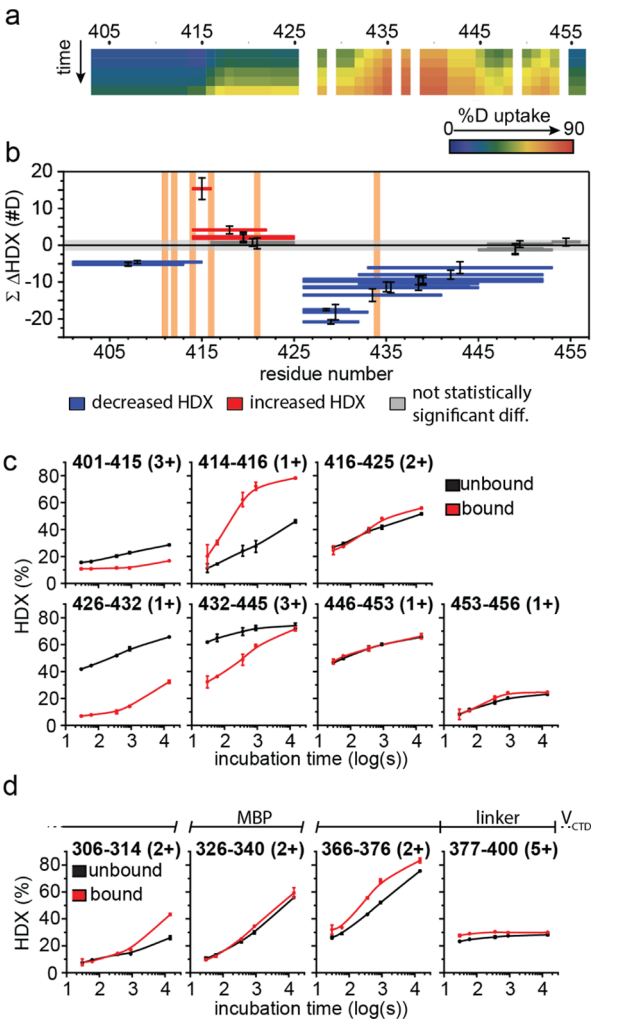

Figure 3. HDX-MS highlights the disordered nature of NiV V_{CTD} and confirms strong binding with $MDA5_{SF2}$. (a) Heat map showing the deuterium uptake extent of free MBP−NiV V_{CTD}. HDX-MS of unbound MBP−NiV V_{CTD} after 10 s through 14,400 s, where the extent of deuterium incorporation is indicated by using the color gradient. (b) Woods' plot showing peptide-level HDX differences between unbound MBP−NiV V_{CTD} and $MDA5_{SF2}$-bound MBP−NiV V_{CTD}. The horizontal bars depict each peptide length spanning a region of the sequence and showing cumulative differences in absolute deuterium uptake between the bound *vs* unbound state of NiV V_{CTD}. Decreases in deuterium uptake are shown as negative values (blue), and increases are shown as positive values (red). Gray shading indicates the global significance range ($p < 0.01$) for which differences are considered statistically significant. Those peptides not reporting a significant difference are shown in dark gray. Error bars depict the propagated error in technical duplicate measurements across all time points. Vertical orange shading shows previously reported binding residues from the PIV5 binding study and sequence alignment. (c) Representative HDX kinetic plots showing peptides covering NiV V_{CTD}. Unbound NiV V_{CTD} (black) *vs* NiV V_{CTD} bound with the $MDA5_{SF2}$ domain (red). (d) Representative kinetic plots showing HDX differences observed of the N-terminal MBP tag. Kinetic plots are shown for the MBP tag region of MHT-NiV V_{CTD} for free MBP−NiV V_{CTD} (black) *vs* MBP−NiV V-CTD co-expressed with the $MDA5_{SF2}$ domain (red). The bar given above shows the identity of the peptide with reference to the composition of the protein construct.

https://doi.org/10.1021/acsinfecdis.1c00403
ACS Infect. Dis. 2022, 8, 118−128

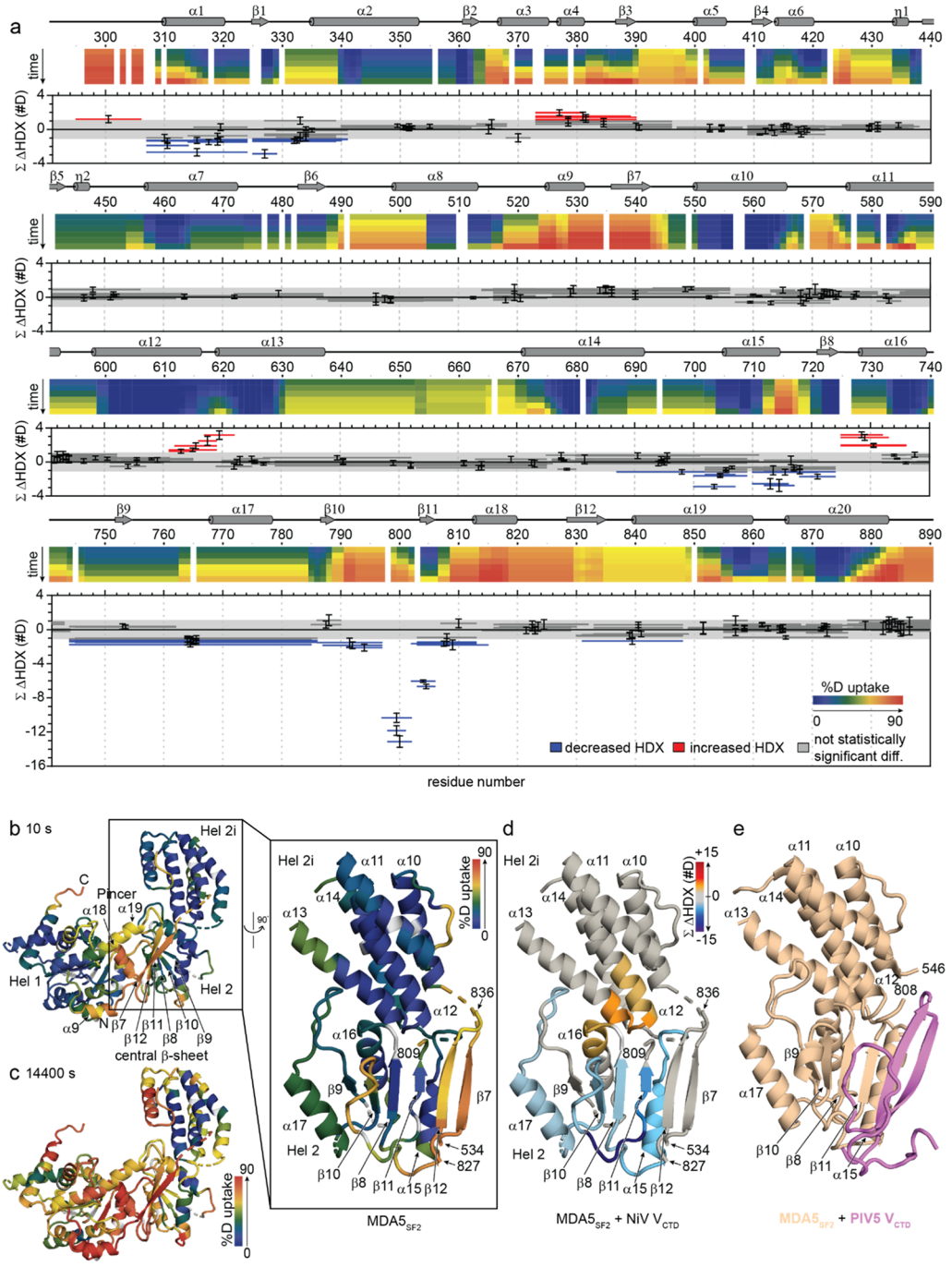

Figure 4. HDX-MS reveals changes in solvent accessibility in the $MDA5_{SF2}$ structure when compared to the $MDA5_{SF2}$/NiV V_{CTD} complex. (a) Heat map showing the deuterium uptake extent of free $MDA5_{SF2}$ relative to secondary structural elements (top) combined with segmented Woods' plot showing peptide-level HDX differences between unbound $MDA5_{SF2}$ and $MDA5_{SF2}$ bound with MBP−NiV V_{CTD} (bottom). HDX of the unbound $MDA5_{SF2}$ construct after 10 s through 14,400 s deuterium exchange times, where deuterium incorporation is indicated using a color scale. Secondary structures extracted from the dsRNA-bound $MDA5_{SF2}$ crystal structure (PDB 4GL2) are shown above for reference. In the Woods' plot, the horizontal bars depict each peptide spanning a region of the sequence and showing cumulative differences in absolute deuterium uptake between the bound and unbound states of the $MDA5_{SF2}$ domain. Decreases in differential deuterium uptake are shown as negative values (blue), and increases are shown as positive values (red). Gray shading indicates the global significance range ($p < 0.01$) for which differences are considered statistically significant. Those peptides not reporting a significant difference are shown in gray. Error bars depict the propagated error in technical duplicate measurements across all time points. (b) HDX of free $MDA5_{SF2}$ after 10 s of HDX mapped onto the $MDA5_{SF2}$ structure. The % HDX was mapped onto the $MDA5_{SF2}$ in the crystal structure bound to dsRNA (PDB 4GL2, ΔCTD, left) and onto $MDA5_{SF2}$ (displaying residues 534−809 and827−836) rotated 90° (right). The HDX extent is indicated by the scale bar to the right: n.d., not determined deuterium uptake due to limited peptide coverage (white). (c) Deuterium uptake of free $MDA5_{SF2}$ after 14,400 s of HDX mapped onto the $MDA5_{SF2}$ structure. The % HDX was mapped onto the $MDA5_{SF2}$ in the crystal structure bound to dsRNA (PDB 4GL2, ΔCTD, left). (d) Peptide-level differential HDX mapped to the dsRNA-bound MDA5 crystal structure. The statistically significant differential HDX for representative peptides shown in a (bottom) were mapped onto the dsRNA-bound $MDA5_{SF2}$ (displaying residues 534−809 and827−836) structure as shown in (b) (right). Differential HDX is indicated by the color bar. (e) Comparison with the PIV5 V_{CTD}-bound $MDA5_{SF2}$ Hel2 and Hel2i crystal structure (PDB 4I1S).

https://doi.org/10.1021/acsinfecdis.1c00403
ACS Infect. Dis. 2022, 8, 118−128

residues C427, C431, C443, and C445, which form the second Zn finger, that are more protected from HDX upon $MDA5_{SF2}$ binding. Our results here confirm that regions encompassing the central cysteine residues are important for binding to MDA5.

Given that our NiV V_{CTD} is fused to an MBP-tag, we wanted to rule out the possibility that MBP was binding to MDA5. Most regions of the MBP tag show little to no statistically significant differences between MBP−NiV V_{CTD} unbound or bound with the $MDA5_{SF2}$ domain (Figure 3d). However, some regions of the MBP-tag show increased HDX, including the region encompassing the His_6-tag and linker residues, which may be a result of steric effects between the larger MBP molecule and NiV V_{CTD}; these interactions are lost when MBP−NiV V_{CTD} is bound to the $MDA5_{SF2}$ domain. This would manifest as an increase in HDX of some regions on NiV V_{CTD} when comparing to the bound complex. Thus, the importance of the N-terminus of NiV V_{CTD}, where the low HDX in the free state (residues 405−425) may be caused by the presence of MBP, is underestimated, and the observed large increase in the exposure of NiV V_{CTD} in the free state (residues 415−422) is likely to be a consequence of the MBP-tag. While previous studies demonstrated the importance of residue I414 in interference with MDA5 activity,[45] we cannot draw conclusions confirming or refuting the importance of I414; however, it is clear that the intrinsically disordered V_{CTD} adopts a more ordered structure, especially with respect to the second Zn finger, in a relatively static binding interaction with $MDA5_{SF2}$.

NiV V_{CTD} Binds and Modulates $MDA5_{SF2}$ Dynamics. Peptic digestion and bottom-up analysis of the $MDA5_{SF2}$ domain, containing Hel1, Hel2, Hel2i, and pincer domains, produced 237 unique peptides (Figure S2b). Most of the $MDA5_{SF2}$ showed low HDX rates, consistent with the high α helical content reported in the crystal structure (PDB 4GL2) (Figure 4a,b). Several regions, however, showed high deuterium exchange rates in parts of Hel2 (β7 and β12 of the central β-sheet region and α18), Hel1 (α9), and pincer (α19) domains, even early in the HDX experiment (Figure 4a,b), suggesting that these regions are more dynamic and conformationally flexible than those reported in the dsRNA-bound $MDA5_{SF2}$ crystal structure. This is consistent with the role of SF2 domains in binding RNA and adenosine 5′-triphosphate that were described previously.[54−56] Interestingly, the central β sheet shows mixed dynamic motion; we observed low HDX for β9, β10, and β8 throughout the experiment, low HDX for β11 at short times that increases with longer times, and high HDX for β12 and β7 even after short times [Figure 4b (inset)]. After 4 h of HDX, the Hel1, Pincer, and part of the Hel2 domains eventually accumulate a high degree of deuterium, but the Hel2i domain remains largely unexchanged, suggesting little conformational diversity and dynamic motion of this α-helix bundle (Figure 4c).

We next evaluated the $MDA5_{SF2}$ domain in the context of the $MDA5_{SF2}$/MBP−NiV V_{CTD} complex. Binding to MBP−NiV V_{CTD} resulted in both increases and decreases in HDX of several regions of the $MDA5_{SF2}$ domain, as shown in the Woods' differential HDX plot (Figure 4a). Within the Hel1 domain, decreased HDX is observed in the regions of α1 through β1 (residues 306−328), whereas increased HDX is observed around α3 through α4 (residues 373−382). The most pronounced difference in HDX is the protection observed in the Hel2 domain (Figure 4a,d) on the periphery of the slow exchanging core noted in the free state (Figure 4b); the largest decreases in HDX are clustered around the region surrounding β11, including α17 through β10 and β11 (residues 763−806), and the flexible region between α14 and α15 through β8 (residues 700−724) (Figure 4a,d). Note that the long peptides encompassing residues 744−784 and covering α17 show decreased HDX, but the shorter peptides encompassing residues 744−762 and before α17 do not. Interestingly, the more dynamic β-strands, β7 and β12, show no evidence of differential HDX within the $MDA5_{SF2}$ domain/MBP−NiV V_{CTD} complex. Overall, all these observations are consistent with the crystal structure of $MDA5_{SF2}$ Hel2 and Hel2i domains in complex with the V protein of another paramyxovirus, PIV5 (Figure 4e).[18] PIV5 V protein displaces the $MDA5_{SF2}$ β7 and β12 in the Hel2 domain and forms a continuous β-sheet with β11. Comparison of our cumulative differential HDX results for the $MDA5_{SF2}$/MBP−NiV V_{CTD} complex with the $MDA5_{SF2}$/PIV5 V structure (PDB 4I1S) reveals that the same decreased HDX around β11 observed in the presence of NiV V_{CTD} would be expected for the PIV5 V protein (Figure 4d,e), suggesting that like the PIV5 V protein, NiV V_{CTD} likely binds to these regions adjacent to Hel2 and pincer domains, causing HDX protection.

MDA5 regions with increased HDX are also observed in the $MDA5_{SF2}$/MBP−NiV V_{CTD} complex, in particular at the ends of α-helices at the interface between Hel2 and Hel2i (Figure 4a,d). Increased HDX, suggesting increased dynamics or solvent exposure, occurs upon binding between α12 and α13 (residues 610−622) and between β8 and α16 (residues 725−732). In other words, these regions show relatively less HDX in the unbound state with the exception of the linker regions already reported in the crystal structure (Figure 4a,b), indicating that they undergo conformation changes distal to the binding sites, and these changes open the structure.[57] Collectively, our data suggest that NiV V_{CTD} not only binds $MDA5_{SF2}$ similar to the PIV5 V protein but also induces changes in the dynamics in other regions within MDA5; these latter changes may impact its antiviral activity.

DISCUSSION

The NiV V protein is a critical virulence factor that potently inhibits host innate immune responses.[22−25] The importance of the NiV V protein in this process was established by earlier studies where $rNiV_M$ strains deficient in the V protein failed to suppress immune responses and caused disease in an animal model.[23] The NiV V protein directly binds to the PRR MDA5 to prevent IFN signaling.[34,35,43,46,47] To develop a better understanding of the role of NiV V in this process, we performed a biochemical and structural characterization of the interaction between NiV V and MDA5. Co-IP assays demonstrated that the NiV V_{CTD} binds to the $MDA5_{SF2}$ domain when co-transfected and not to other domains. *In vitro* pulldown assays using purified recombinant proteins and co-purification of cell lysates containing individually expressed proteins do not show direct interactions. However, co-expression and co-purification of the recombinant MBP−NiV V_{CTD}/$MDA5_{SF2}$ domain complex provide evidence of a soluble, intact complex. This is not surprising as heterologous protein overexpression in *E. coli* can result in misfolded or insoluble proteins. Several factors contribute to the production of stable proteins, including cofactors and post-translational modifications, which may be absent in *E. coli*. Co-expression with a binding partner can help overcome some of these

https://doi.org/10.1021/acsinfecdis.1c00403
ACS Infect. Dis. 2022, 8, 118−128

barriers and facilitate production of functional proteins by reducing conformational flexibility.[58] Moreover, the NiV V protein has been recently described as an intrinsically disordered protein (IDP) that lacks a significantly folded structure and conformational stability.[48] IDPs like the NiV V protein can undergo binding-induced folding during complex formation that is dependent on the nature of the binding partner.[59−61] Thus, co-expression and co-translation in a recombinant system can generate complexes that may not form by mixing individual components, especially when involving IDPs.

Structural analysis of the co-expressed and co-purified NiV V_{CTD}/$MDA5_{SF2}$ domain complex revealed extensive HDX protection throughout NiV V_{CTD}. Differential HDX-MS analysis for residues covering residues 408−415 and 426−432 indicates static binding with $MDA5_{SF2}$ (*i.e.*, low on−off rates). A region encompassing residues 433−445 suggests weaker bonding or a more dynamic interaction with nearby $MDA5_{SF2}$ residues (*i.e.*, higher off rates). The importance of conserved residues R409, E411, I414, and C431 that attenuate NiV V binding to MDA5[45] is consistent with the static localized binding shown by the HDX-MS analysis; C443 and C445 are within the more dynamic binding site, but there is no evidence of C448 participation. Notably, these regions also cover the four central cysteine residues that form the second zinc finger (*i.e.*, C427, C431, C443, and C445). While these results cannot confirm the importance of the cysteine side chains, the HDX results are evidence of direct binding of these regions with $MDA5_{SF2}$ or binding-induced stabilization of the intrinsically disordered unbound V_{CTD} backbone. Despite this observation, addition of EDTA did not disrupt the interaction between NiV V_{CTD} and $MDA5_{SF2}$, suggesting that the Zn motif is either protected within the complex or that higher concentrations are needed to extract the zinc ions.

HDX-MS analysis of free $MDA5_{SF2}$ is largely consistent with the reported crystal structure of $MDA5_{SF2}$ bound to dsRNA;[54,62] however, the HDX data also identified a highly exchanging region comprising β7, β12, and α18 of the Hel2 domain, α9 of the Hel1 domain, and much of α19 of the pincer domain. The extensive HDX observed for β7 and β12 at short times and that observed for β11 at longer times indicates that this β-sheet structure is not static in the free state but rather very dynamic.

Differential HDX-MS analysis of NiV V_{CTD} binding to the $MDA5_{SF2}$ domain indicates a relatively static binding interaction covering the vicinity of β11 (Figure 4) but no effect on the dynamic strands of the β-sheet region, β7 and β12. The location of this binding site is interesting because if the β-sheet structure is maintained in the unbound state, binding-induced protection should not be observed for β11. The lack of statistically significant differences in HDX between bound and unbound within this dynamic region indicates that this region is locked in an exposed or open conformation.

There are significant parallels to what we observe by HDX-MS of the NiV V_{CTD}/$MDA5_{SF2}$ domain complex and the reported crystal structure of PIV5 V_{CTD}/$MDA5_{SF2}$ (PDB 4I1S). In the PIV5 V_{CTD}/$MDA5_{SF2}$ structure, the PIV5 V_{CTD} replaces the $MDA5_{SF2}$ β7 and β12 strands in the central β-sheet. PIV5 V binding with $MDA5_{SF2}$ is associated with decreased formation of RNA-bound signaling MDA5 oligomers, possibly disrupting SF2−SF2 or SF2−RNA-binding domain interactions.[18] The results reported here are consistent with NiV V_{CTD}, similarly displacing the $MDA5_{SF2}$ β7 and β12 strands. Furthermore, the HDX results suggest that this displacement does not change the conformational preference of the $MDA5_{SF2}$ β-strands from the RNA-free unbound state but would prevent formation of the central β-sheet observed in the RNA-bound $MDA5_{SF2}$ crystal structure (PDB 4GL2).[54] This suggests that NiV V may sterically hinder "closing" of the RNA-free dynamic conformation of $MDA5_{SF2}$.

Our HDX-MS results revealed binding-induced conformational changes in regions distal to the binding interface of NiV V_{CTD}/$MDA5_{SF2}$ that may have additional implications for $MDA5_{SF2}$ binding with dsRNA. Regions near α13 and α14 of the Hel2i subdomain and α6 of the Hel2 subdomain show increased HDX when $MDA5_{SF2}$ is bound to NiV V_{CTD}, indicating either a binding-induced decrease in the α-helical character and/or an increase in dynamic motion. We observe decreased HDX of a remote region near α17 of the Hel2 subdomain and α1 and β1 of the Hel1 domain and some exposure near α3 and α4. These remote conformational changes present important potential implications for NiV V_{CTD} binding with the $MDA5_{SF2}$ domain, wherein NiV V_{CTD} may impede dsRNA binding to the $MDA5_{SF2}$ domain despite its remote binding site. Thus, our HDX results indicate that the NiV V protein binding site on the $MDA5_{SF2}$ domain is similar but not entirely the same as that of PIV5 V.[18,46]

We have shown here that the β-sheet region within the $MDA5_{SF2}$ domain is dynamic, and the regions at the interface become protected upon binding with NiV V_{CTD}. Formation of the NiV V_{CTD}/$MDA5_{SF2}$ domain complex stabilizes the V_{CTD}, including in the region encompassing the conserved central cysteine residues, and leads to allosteric changes in MDA5 that likely disrupts its activity. Thus, modulation of the conformational dynamics within MDA5 may present a potential mechanism for immune evasion by a highly pathogenic RNA virus.

METHODS

Recombinant Protein Production. The gene encoding the NiV V protein (accession AAK50551) was codon-optimized for expression in *E. coli* (GeneScript, NJ) prior to subcloning into a modified pET15b plasmid containing a maltose-binding protein (MBP) tag followed by a His_6 tag. MDA5 and $MDA5_{SF2}$ were amplified from human complementary DNA by polymerase chain reaction. All sequences were confirmed with Sanger sequencing. Recombinant proteins were expressed in *E. coli* BL21(DE3) cells at 18 °C for 16 h with 0.25 mM IPTG induction. Cells were pelleted down by centrifugation and re-suspended in lysis buffer containing 50 mM Tris-HCl (pH 8.0), 300 mM NaCl, and protease inhibitors prior to lysis with an EmulsiFlex-C5 homogenizer (Avestin, Canada). Lysate was clarified by centrifugation at 60,000*g* and then used for pulldown assays or further protein purification using a series of affinity, ion exchange, and gel filtration columns (GE Healthcare, IL). The MBP-tag on $MDA5_{SF2}$ was cleaved using TEV protease and removed by affinity purification. Final protein samples were assessed by SDS-PAGE.

Co-immunoprecipitation. HEK293T cells were grown in 6-well plates in Dulbecco's modified Eagle medium containing 10% fetal bovine serum. Cells were transfected at approximately 80% confluency with a mixture of one plasmid encoding NiV proteins and the other encoding MDA5 protein for co-IP experiments. Cells were harvested by centrifugation at 48 h after transfection. After washing once with phosphate-

https://doi.org/10.1021/acsinfecdis.1c00403
ACS Infect. Dis. 2022, 8, 118−128

buffered saline, cells were either stored in −80 °C for use or suspended in lysis buffer containing 50 mM Tris-HCl, pH 8.0, 280 mM NaCl, 2 mM EGTA, 0.4 mM EDTA, 10% glycerol, 0.5% IGEPAL CA630 (Sigma-Aldrich), and a protease inhibitor cocktail. The lysate was clarified with centrifugation at 14,000 rpm for 15 min, and the clarification was repeated three times. The resultant supernatant, WCE hereafter, was used to incubate with anti-FLAG M2 magnetic beads (Sigma-Aldrich, M8823) at 4 °C. The beads were pelleted down using a magnetic rack after 1 h of incubation and washed five times with the lysis buffer. Proteins bound on the beads were eluted with 150 ng/mL FLAG peptide (Sigma-Aldrich, F3290). Samples from the WCE and the elution were transferred to the poly(vinylidene difluoride) membrane for Western blot after resolving by SDS-PAGE. Mouse anti-FLAG (F3165) and anti-HA (Sigma-Aldrich, H3663) monoclonal antibodies were used as primary antibodies to detect viral proteins and human proteins with the corresponding epitope, respectively. Goat anti-mouse IgG−HRP conjugated antibody (Santa Cruz, SC-2005) was used as a secondary antibody for the western blot. Blot images were taken from Amersham Imager 600 (GE Healthcare).

MBP Pulldown Assay. MBP pulldown assay was similar to that previously reported.[63] Briefly, *E. coli* lysate clarified by centrifugation or purified proteins was incubated with amylose resin at high flow (New England Biolabs, E8022L) in binding buffer for 30 min with moderate agitation in a cold room. The resin was washed six times with washing buffer and eluted with binding buffer containing 15 mM maltose. Samples were resolved by SDS-PAGE and stained with Coomassie blue for visualization. For co-lysate preparation, cells expressing either the viral protein or human $MDA5_{SF2}$ were re-suspended in lysis buffer containing 150 mM NaCl and mixed before homogenization.

Hydrogen−Deuterium Exchange Mass Spectrometry (HDX-MS). All chemical reagents used in HDX-MS experiments were purchased from Sigma-Aldrich (St. Louis, MO) unless otherwise noted. HDX-MS analyses were carried out, as previously described,[64,65] on purified MBP−NiV V_{CTD}, $MDA5_{SF2}$, and the co-expressed MBP−NiV V-CTD/$MDA5_{SF2}$ protein complex (stock solutions 40 μM per protein in PBS, pH 7.4). Briefly, HDX was initiated by diluting 4 μL of a protein stock solution with a ninefold excess of PBS in D_2O (Cambridge Isotope Laboratories, Inc., Tewksbury, MA) (final composition 90/10% v/v D_2O/H_2O). The mixture was exchanged on ice for 0, 10, 30, 60, 360, 900, or 144,000 s, and the HDX was quenched by adding 30 μL of a quench buffer (3 M urea in PBS, pH 2.4). In-solution digestion was performed using protease type XIII from *Aspergillus saitoi* (fungal XIII, PBS pH 2.4) immediately after quenching and incubated for 3 min at 22 °C.

All liquid chromatography/mass spectrometry (LC/MS) analyses were performed using a custom-built liquid chromatography (LC) assembly coupled to an LTQ-FTICR mass spectrometer (Thermo Fisher, Waltham, MA). The LC system incorporated online pepsin protease digestion using a custom-prepared immobilized pepsin column (2 × 20 mm), followed by peptide trapping and desalting on a ZORBAX Eclipse XDB C8 column (2.1 × 15 mm, Agilent, Santa Clara, CA) and reversed-phase peptide separation with an XSelect CSH C18 column (2.1 × 50 mm, Waters, Manchester, UK). All HDX-MS time points were analyzed in duplicate.

Using the same setup and procedure, proteolytic mapping analyses were performed prior to HDX on nondeuterated aliquots of the protein stock solutions, except that tandem MS in the data-dependent mode was used. The top six most abundant fragment ions from each scan were selected for MS/MS analysis. The MS/MS files were analyzed using Byonic and Byologic (Protein Metrics, San Carlos, CA) to generate a list of identified peptides to be followed in the HDX-MS analyses. The search was also carried out against reverse sequences of the proteins to discard ambiguous assignments.

All HDX-MS analyses were processed using HDExaminer (version 2.5.1, Sierra Analytics, Modesto, CA); adjustment of LC boundaries and validation of MS interferences were performed manually on all peptides. Woods' plot peptide cumulative HDX differences were calculated as the sum of all differences at all time points in daltons $[\sum(D_{coexpressed}) - \sum(D_{free})]$. The standard errors of the mean were propagated through the calculation and shown as error bars. The global significance limit was calculated as previously described.[66,67] Briefly, the pooled standard deviation was calculated for all time points and all peptides within each state (*i.e.*, bound and unbound). The pooled standard deviations were used to calculate the population standard error of the mean, and this standard error was used with a two-tailed *t*-test value ($p < 0.01$) to calculate the confidence interval distribution for differences in HDX across the dataset. Statistically significant differences for representative peptides were mapped onto structures using PyMOL. For a summary of all HDX data, see the Supporting Information.

■ ASSOCIATED CONTENT

Supporting Information

The Supporting Information is available free of charge at https://pubs.acs.org/doi/10.1021/acsinfecdis.1c00403.

Western blot images, coverage maps for HDX-MS, additional views of the HDX-MS results mapped onto the structures, and compilation of raw HDX values (PDF)

■ AUTHOR INFORMATION

Corresponding Author

Daisy W. Leung − *Division of Infectious Diseases, John T. Milliken Department of Medicine and Department of Pathology and Immunology, Washington University School of Medicine, St. Louis, Missouri 63110, United States;* orcid.org/0000-0002-7189-9557; Email: dwleung@wustl.edu

Authors

Nicole D. Wagner − *Division of Infectious Diseases, John T. Milliken Department of Medicine, Washington University School of Medicine, St. Louis, Missouri 63110, United States; Department of Chemistry, Washington University in St. Louis, St. Louis, Missouri 63130, United States;* orcid.org/0000-0003-3980-4893

Hejun Liu − *Division of Infectious Diseases, John T. Milliken Department of Medicine and Department of Pathology and Immunology, Washington University School of Medicine, St. Louis, Missouri 63110, United States;* Present Address: Department of Integrative Structural and Computational Biology, The Scripps Research Institute, La Jolla, CA 92037, USA

https://doi.org/10.1021/acsinfecdis.1c00403
ACS Infect. Dis. 2022, 8, 118−128

Henry W. Rohrs − *Department of Chemistry, Washington University in St. Louis, St. Louis, Missouri 63130, United States*

Gaya K. Amarasinghe − *Department of Pathology and Immunology, Washington University School of Medicine, St. Louis, Missouri 63110, United States;* orcid.org/0000-0002-0418-9707

Michael L. Gross − *Department of Chemistry, Washington University in St. Louis, St. Louis, Missouri 63130, United States;* orcid.org/0000-0003-1159-4636

Complete contact information is available at: https://pubs.acs.org/10.1021/acsinfecdis.1c00403

Author Contributions

△N.D.W. and H.L. contributed equally. D.W.L. and G.K.A. conceived the project. D.W.L., G.K.A., and M.L.G. designed the experimental plans. H.L. generated samples. H.L., N.D.W., and H.W.R. performed experiments and analyzed results. H.L. wrote an initial draft manuscript with N.D.W. N.D.W. analyzed data and completed manuscript. N.D.W., M.L.G., G.K.A., and D.W.L. participated in editing the final version of the manuscript.

Notes

The authors declare no competing financial interest.

■ ACKNOWLEDGMENTS

This work was supported by grants from the NIH (R01AI140758 to D.W.L.; P41 GM103422 and R24GM136766 to M.L.G.; and P01AI120943 and R01AI109945 to G.K.A.). We thank members of the Amarasinghe, Gross, and Leung laboratories for support and comments.

■ REFERENCES

(1) Farrar, J. J. Nipah-virus encephalitis-investigation of a new infection. *Lancet* **1999**, *354*, 1222−1223.

(2) Chua, K. B.; Bellini, W. J.; Rota, P. A.; Harcourt, B. H.; Tamin, A.; Lam, S. K.; Ksiazek, T. G.; Rollin, P. E.; Zaki, S. R.; Shieh, W.-J.; Goldsmith, C. S.; Gubler, D. J.; Roehrig, J. T.; Eaton, B.; Gould, A. R.; Olson, J.; Field, H.; Daniels, P.; Ling, A. E.; Peters, C. J.; Anderson, L. J.; Mahy, B. W. J. Nipah virus: a recently emergent deadly paramyxovirus. *Science* **2000**, *288*, 1432−1435.

(3) Sarji, S. A.; Abdullah, B. J. J.; Goh, K. J.; Tan, C. T.; Wong, K. T. MR imaging features of Nipah encephalitis. *AJR, Am. J. Roentgenol.* **2000**, *175*, 437−442.

(4) Pelissier, R.; Iampietro, M.; Horvat, B. Recent advances in the understanding of Nipah virus immunopathogenesis and anti-viral approaches. *F1000Research* **2019**, *8*, F1000.

(5) Anam, A. M.; Ahmad, J.; Huq, S. M. R.; Rabbani, R. Nipah virus encephalitis: MRI findings. *J. R. Coll. Physicians Edinb.* **2019**, *49*, 227−228.

(6) Clayton, B. A. Nipah virus: transmission of a zoonotic paramyxovirus. *Curr. Opin. Virol.* **2017**, *22*, 97−104.

(7) Epstein, J. H.; Field, H. E.; Luby, S.; Pulliam, J. R. C.; Daszak, P. Nipah virus: impact, origins, and causes of emergence. *Curr. Infect. Dis. Rep.* **2006**, *8*, 59−65.

(8) Harcourt, B. H.; Lowe, L.; Tamin, A.; Liu, X.; Bankamp, B.; Bowden, N.; Rollin, P. E.; Comer, J. A.; Ksiazek, T. G.; Hossain, M. J.; Gurley, E. S.; Breiman, R. F.; Bellini, W. J.; Rota, P. A. Genetic characterization of Nipah virus, Bangladesh, 2004. *Emerging Infect. Dis.* **2005**, *11*, 1594−1597.

(9) Mire, C. E.; Satterfield, B. A.; Geisbert, J. B.; Agans, K. N.; Borisevich, V.; Yan, L.; Chan, Y.-P.; Cross, R. W.; Fenton, K. A.; Broder, C. C.; Geisbert, T. W. Pathogenic Differences between Nipah Virus Bangladesh and Malaysia Strains in Primates: Implications for Antibody Therapy. *Sci. Rep.* **2016**, *6*, 30916.

(10) Wang, L.-F.; Harcourt, B. H.; Yu, M.; Tamin, A.; Rota, P. A.; Bellini, W. J.; Eaton, B. T. Molecular biology of Hendra and Nipah viruses. *Microbes Infect.* **2001**, *3*, 279−287.

(11) Marsh, G. A.; de Jong, C.; Barr, J. A.; Tachedjian, M.; Smith, C.; Middleton, D.; Yu, M.; Todd, S.; Foord, A. J.; Haring, V.; Payne, J.; Robinson, R.; Broz, I.; Crameri, G.; Field, H. E.; Wang, L.-F. Cedar virus: a novel Henipavirus isolated from Australian bats. *PLoS Pathog.* **2012**, *8*, No. e1002836.

(12) Wu, Z.; Yang, L.; Yang, F.; Ren, X.; Jiang, J.; Dong, J.; Sun, L.; Zhu, Y.; Zhou, H.; Jin, Q. Novel Henipa-like virus, Mojiang Paramyxovirus, in rats, China, 2012. *Emerging Infect. Dis.* **2014**, *20*, 1064−1066.

(13) Amarasinghe, G. K.; Ayllón, M. A.; Bào, Y.; Basler, C. F.; Bavari, S.; Blasdell, K. R.; Briese, T.; Brown, P. A.; Bukreyev, A.; Balkema-Buschmann, A.; Buchholz, U. J.; Chabi-Jesus, C.; Chandran, K.; Chiapponi, C.; Crozier, I.; de Swart, R. L.; Dietzgen, R. G.; Dolnik, O.; Drexler, J. F.; Dürrwald, R.; Dundon, W. G.; Duprex, W. P.; Dye, J. M.; Easton, A. J.; Fooks, A. R.; Formenty, P. B. H.; Fouchier, R. A. M.; Freitas-Astúa, J.; Griffiths, A.; Hewson, R.; Horie, M.; Hyndman, T. H.; Jiāng, D.; Kitajima, E. W.; Kobinger, G. P.; Kondō, H.; Kurath, G.; Kuzmin, I. V.; Lamb, R. A.; Lavazza, A.; Lee, B.; Lelli, D.; Leroy, E. M.; Lǐ, J.; Maes, P.; Marzano, S.-Y. L.; Moreno, A.; Mühlberger, E.; Netesov, S. V.; Nowotny, N.; Nylund, A.; Økland, A. L.; Palacios, G.; Pályi, B.; Pawęska, J. T.; Payne, S. L.; Prosperi, A.; Ramos-González, P. L.; Rima, B. K.; Rota, P.; Rubbenstroth, D.; Shī, M.; Simmonds, P.; Smither, S. J.; Sozzi, E.; Spann, K.; Stenglein, M. D.; Stone, D. M.; Takada, A.; Tesh, R. B.; Tomonaga, K.; Tordo, N.; Towner, J. S.; van den Hoogen, B.; Vasilakis, N.; Wahl, V.; Walker, P. J.; Wang, L.-F.; Whitfield, A. E.; Williams, J. V.; Zerbini, F. M.; Zhāng, T.; Zhang, Y.-Z.; Kuhn, J. H. Taxonomy of the order Mononegavirales: update 2019. *Arch. Virol.* **2019**, *164*, 1967−1980.

(14) Park, M.-S.; Shaw, M. L.; Munoz-Jordan, J.; Cros, J. F.; Nakaya, T.; Bouvier, N.; Palese, P.; Garcia-Sastre, A.; Basler, C. F. Newcastle disease virus (NDV)-based assay demonstrates interferon-antagonist activity for the NDV V protein and the Nipah virus V, W, and C proteins. *J. Virol.* **2003**, *77*, 1501−1511.

(15) Kulkarni, S.; Volchkova, V.; Basler, C. F.; Palese, P.; Volchkov, V. E.; Shaw, M. L. Nipah virus edits its P gene at high frequency to express the V and W proteins. *J. Virol.* **2009**, *83*, 3982−3987.

(16) Lo, M. K.; Harcourt, B. H.; Mungall, B. A.; Tamin, A.; Peeples, M. E.; Bellini, W. J.; Rota, P. A. Determination of the henipavirus phosphoprotein gene mRNA editing frequencies and detection of the C, V and W proteins of Nipah virus in virus-infected cells. *J. Gen. Virol.* **2009**, *90*, 398−404.

(17) Shaw, M. Henipaviruses employ a multifaceted approach to evade the antiviral interferon response. *Viruses* **2009**, *1*, 1190−1203.

(18) Motz, C.; Schuhmann, K. M.; Kirchhofer, A.; Moldt, M.; Witte, G.; Conzelmann, K.-K.; Hopfner, K.-P.; Paramyxovirus, V. Paramyxovirus V Proteins Disrupt the Fold of the RNA Sensor MDA5 to Inhibit Antiviral Signaling. *Science* **2013**, *339*, 690−693.

(19) Li, T.; Chen, X.; Garbutt, K. C.; Zhou, P.; Zheng, N. Structure of DDB1 in complex with a paramyxovirus V protein: Viral hijack of a propeller cluster in ubiquitin ligase. *Cell* **2006**, *124*, 105−117.

(20) Liston, P.; Briedis, D. J. Measles virus V protein binds zinc. *Virology* **1994**, *198*, 399−404.

(21) Paterson, R. G.; Leser, G. P.; Shaughnessy, M. A.; Lamb, R. A. The paramyxovirus SV5 V protein binds two atoms of zinc and is a structural component of virions. *Virology* **1995**, *208*, 121−131.

(22) Audsley, M. D.; Moseley, G. W. Paramyxovirus evasion of innate immunity: Diverse strategies for common targets. *World J. Virol.* **2013**, *2*, 57−70.

(23) Satterfield, B. A.; Cross, R. W.; Fenton, K. A.; Agans, K. N.; Basler, C. F.; Geisbert, T. W.; Mire, C. E. The immunomodulating V and W proteins of Nipah virus determine disease course. *Nat. Commun.* **2015**, *6*, 7483.

(24) Yoneda, M.; Guillaume, V.; Sato, H.; Fujita, K.; Georges-Courbot, M.-C.; Ikeda, F.; Omi, M.; Muto-Terao, Y.; Wild, T. F.; Kai,

C. The nonstructural proteins of Nipah virus play a key role in pathogenicity in experimentally infected animals. *PLoS One* **2010**, *5*, No. e12709.
(25) Satterfield, B. A.; Cross, R. W.; Fenton, K. A.; Borisevich, V.; Agans, K. N.; Deer, D. J.; Graber, J.; Basler, C. F.; Geisbert, T. W.; Mire, C. E. Nipah Virus C and W Proteins Contribute to Respiratory Disease in Ferrets. *J. Virol.* **2016**, *90*, 6326−6343.
(26) Ramos, H. J.; Gale, M., Jr. RIG-I like receptors and their signaling crosstalk in the regulation of antiviral immunity. *Curr. Opin. Virol.* **2011**, *1*, 167−176.
(27) Wilkins, C.; Gale, M., Jr. Recognition of viruses by cytoplasmic sensors. *Curr. Opin. Immunol.* **2010**, *22*, 41−47.
(28) Yoneyama, M.; Kikuchi, M.; Natsukawa, T.; Shinobu, N.; Imaizumi, T.; Miyagishi, M.; Taira, K.; Akira, S.; Fujita, T. The RNA helicase RIG-I has an essential function in double-stranded RNA-induced innate antiviral responses. *Nat. Immunol.* **2004**, *5*, 730−737.
(29) Kang, D.-c.; Gopalkrishnan, R. V.; Wu, Q.; Jankowsky, E.; Pyle, A. M.; Fisher, P. B. mda-5: An interferon-inducible putative RNA helicase with double-stranded RNA-dependent ATPase activity and melanoma growth-suppressive properties. *Proc. Natl. Acad. Sci. U.S.A.* **2002**, *99*, 637−642.
(30) Yoneyama, M.; Kikuchi, M.; Matsumoto, K.; Imaizumi, T.; Miyagishi, M.; Taira, K.; Foy, E.; Loo, Y.-M.; Gale, M., Jr.; Akira, S.; Yonehara, S.; Kato, A.; Fujita, T. Shared and unique functions of the DExD/H-box helicases RIG-I, MDA5, and LGP2 in antiviral innate immunity. *J. Immunol.* **2005**, *175*, 2851−2858.
(31) Miyoshi, K.; Cui, Y.; Riedlinger, G.; Robinson, P.; Lehoczky, J.; Zon, L.; Oka, T.; Dewar, K.; Hennighausen, L. Structure of the mouse Stat 3/5 locus: evolution from Drosophila to zebrafish to mouse. *Genomics* **2001**, *71*, 150−155.
(32) Hur, S. Double-Stranded RNA Sensors and Modulators in Innate Immunity. *Annu. Rev. Immunol.* **2019**, *37*, 349−375.
(33) Andrejeva, J.; Childs, K. S.; Young, D. F.; Carlos, T. S.; Stock, N.; Goodbourn, S.; Randall, R. E. The V proteins of paramyxoviruses bind the IFN-inducible RNA helicase, mda-5, and inhibit its activation of the IFN-beta promoter. *Proc. Natl. Acad. Sci. U.S.A.* **2004**, *101*, 17264−17269.
(34) Childs, K.; Stock, N.; Ross, C.; Andrejeva, J.; Hilton, L.; Skinner, M.; Randall, R.; Goodbourn, S. mda-5, but not RIG-I, is a common target for paramyxovirus V proteins. *Virology* **2007**, *359*, 190−200.
(35) Childs, K. S.; Andrejeva, J.; Randall, R. E.; Goodbourn, S. Mechanism of mda-5 Inhibition by paramyxovirus V proteins. *J. Virol.* **2009**, *83*, 1465−1473.
(36) Rodriguez, J. J.; Parisien, J.-P.; Horvath, C. M. Nipah virus V protein evades alpha and gamma interferons by preventing STAT1 and STAT2 activation and nuclear accumulation. *J. Virol.* **2002**, *76*, 11476−11483.
(37) Rodriguez, J. J.; Cruz, C. D.; Horvath, C. M. Identification of the nuclear export signal and STAT-binding domains of the Nipah virus V protein reveals mechanisms underlying interferon evasion. *J. Virol.* **2004**, *78*, 5358−5367.
(38) Ciancanelli, M. J.; Volchkova, V. A.; Shaw, M. L.; Volchkov, V. E.; Basler, C. F. Nipah virus sequesters inactive STAT1 in the nucleus via a P gene-encoded mechanism. *J. Virol.* **2009**, *83*, 7828−7841.
(39) Shaw, M. L.; Garcia-Sastre, A.; Palese, P.; Basler, C. F. Nipah virus V and W proteins have a common STAT1-binding domain yet inhibit STAT1 activation from the cytoplasmic and nuclear compartments, respectively. *J. Virol.* **2004**, *78*, 5633−5641.
(40) Smith, K. M.; Tsimbalyuk, S.; Edwards, M. R.; Cross, E. M.; Batra, J.; Soares da Costa, T. P.; Aragão, D.; Basler, C. F.; Forwood, J. K. Structural basis for importin alpha 3 specificity of W proteins in Hendra and Nipah viruses. *Nat. Commun.* **2018**, *9*, 3703.
(41) Shaw, M. L.; Cardenas, W. B.; Zamarin, D.; Palese, P.; Basler, C. F. Nuclear localization of the Nipah virus W protein allows for inhibition of both virus- and toll-like receptor 3-triggered signaling pathways. *J. Virol.* **2005**, *79*, 6078−6088.
(42) Sanchez-Aparicio, M. T.; Feinman, L. J.; Garcia-Sastre, A.; Shaw, M. L. Paramyxovirus V proteins interact with the RIG-I/TRIM25 regulatory complex and inhibit RIG-I signaling. *J. Virol.* **2018**, *92*, e01960−17.
(43) Parisien, J.-P.; Bamming, D.; Komuro, A.; Ramachandran, A.; Rodriguez, J. J.; Barber, G.; Wojahn, R. D.; Horvath, C. M. A shared interface mediates paramyxovirus interference with antiviral RNA helicases MDA5 and LGP2. *J. Virol.* **2009**, *83*, 7252−7260.
(44) Childs, K.; Randall, R.; Goodbourn, S. Paramyxovirus V proteins interact with the RNA Helicase LGP2 to inhibit RIG-I-dependent interferon induction. *J. Virol.* **2012**, *86*, 3411−3421.
(45) Ramachandran, A.; Horvath, C. M. Dissociation of paramyxovirus interferon evasion activities: universal and virus-specific requirements for conserved V protein amino acids in MDA5 interference. *J. Virol.* **2010**, *84*, 11152−11163.
(46) Rodriguez, K. R.; Horvath, C. M. Amino acid requirements for MDA5 and LGP2 recognition by paramyxovirus V proteins: a single arginine distinguishes MDA5 from RIG-I. *J. Virol.* **2013**, *87*, 2974−2978.
(47) Rodriguez, K. R.; Horvath, C. M. Paramyxovirus V protein interaction with the antiviral sensor LGP2 disrupts MDA5 signaling enhancement but is not relevant to LGP2-mediated RLR signaling inhibition. *J. Virol.* **2014**, *88*, 8180−8188.
(48) Schiavina, M.; Salladini, E.; Murrali, M. G.; Tria, G.; Felli, I. C.; Pierattelli, R.; Longhi, S. Ensemble description of the intrinsically disordered N-terminal domain of the Nipah virus P/V protein from combined NMR and SAXS. *Sci. Rep.* **2020**, *10*, 19574.
(49) Horvath, C. M. Weapons of STAT destruction. Interferon evasion by paramyxovirus V protein. *Eur. J. Biochem.* **2004**, *271*, 4621−4628.
(50) Angers, S.; Li, T.; Yi, X.; MacCoss, M. J.; Moon, R. T.; Zheng, N. Molecular architecture and assembly of the DDB1-CUL4A ubiquitin ligase machinery. *Nature* **2006**, *443*, 590−593.
(51) Chalmers, M. J.; Busby, S. A.; Pascal, B. D.; West, G. M.; Griffin, P. R. Differential hydrogen/deuterium exchange mass spectrometry analysis of protein-ligand interactions. *Expert Rev. Proteomics* **2011**, *8*, 43−59.
(52) Weis, D. D. *Hydrogen Exchange Mass Spectrometry of Proteins: Fundamentals, Methods, and Applications*; Wiley: Chichester, West Sussex, 2016; p 1 online resource.
(53) Masson, G. R.; Burke, J. E.; Ahn, N. G.; Anand, G. S.; Borchers, C.; Brier, S.; Bou-Assaf, G. M.; Engen, J. R.; Englander, S. W.; Faber, J.; Garlish, R.; Griffin, P. R.; Gross, M. L.; Guttman, M.; Hamuro, Y.; Heck, A. J. R.; Houde, D.; Iacob, R. E.; Jørgensen, T. J. D.; Kaltashov, I. A.; Klinman, J. P.; Konermann, L.; Man, P.; Mayne, L.; Pascal, B. D.; Reichmann, D.; Skehel, M.; Snijder, J.; Strutzenberg, T. S.; Underbakke, E. S.; Wagner, C.; Wales, T. E.; Walters, B. T.; Weis, D. D.; Wilson, D. J.; Wintrode, P. L.; Zhang, Z.; Zheng, J.; Schriemer, D. C.; Rand, K. D. Recommendations for performing, interpreting and reporting hydrogen deuterium exchange mass spectrometry (HDX-MS) experiments. *Nat. Methods* **2019**, *16*, 595−602.
(54) Wu, B.; Peisley, A.; Richards, C.; Yao, H.; Zeng, X.; Lin, C.; Chu, F.; Walz, T.; Hur, S. Structural basis for dsRNA recognition, filament formation, and antiviral signal activation by MDA5. *Cell* **2013**, *152*, 276−289.
(55) Rawling, D. C.; Pyle, A. M. Parts, assembly and operation of the RIG-I family of motors. *Curr. Opin. Struct. Biol.* **2014**, *25*, 25−33.
(56) Kowalinski, E.; Lunardi, T.; McCarthy, A. A.; Louber, J.; Brunel, J.; Grigorov, B.; Gerlier, D.; Cusack, S. Structural basis for the activation of innate immune pattern-recognition receptor RIG-I by viral RNA. *Cell* **2011**, *147*, 423−435.
(57) Englander, S. W. Hydrogen exchange and mass spectrometry: A historical perspective. *J. Am. Soc. Mass Spectrom.* **2006**, *17*, 1481−1489.
(58) Tolia, N. H.; Joshua-Tor, L. Strategies for protein coexpression in Escherichia coli. *Nat. Methods* **2006**, *3*, 55−64.
(59) Arai, M.; Sugase, K.; Dyson, H. J.; Wright, P. E. Conformational propensities of intrinsically disordered proteins influence the mechanism of binding and folding. *Proc. Natl. Acad. Sci. U.S.A.* **2015**, *112*, 9614−9619.

https://doi.org/10.1021/acsinfecdis.1c00403
ACS Infect. Dis. 2022, 8, 118−128

(60) Toto, A.; Malagrinò, F.; Visconti, L.; Troilo, F.; Pagano, L.; Brunori, M.; Jemth, P.; Gianni, S. Templated folding of intrinsically disordered proteins. *J. Biol. Chem.* **2020**, *295*, 6586−6593.
(61) Uversky, V. N. Paradoxes and wonders of intrinsic disorder: Stability of instability. *Intrinsically Disord. Proteins* **2017**, *5*, No. e1327757.
(62) Uchikawa, E.; Lethier, M.; Malet, H.; Brunel, J.; Gerlier, D.; Cusack, S. Structural Analysis of dsRNA Binding to Anti-viral Pattern Recognition Receptors LGP2 and MDA5. *Mol. Cell* **2016**, *62*, 586−602.
(63) Liu, H.; Zhang, M.; He, W.; Zhu, Z.; Teng, M.; Gao, Y.; Niu, L. Structural insights into yeast histone chaperone Hif1: a scaffold protein recruiting protein complexes to core histones. *Biochem. J.* **2014**, *462*, 465−473.
(64) Ramakrishnan, D.; Xing, W.; Beran, R. K.; Chemuru, S.; Rohrs, H.; Niedziela-Majka, A.; Marchand, B.; Mehra, U.; Zabransky, A.; Dolezal, M.; Hubalek, M.; Pichova, I.; Gross, M. L.; Kwon, H. J.; Fletcher, S. P. Hepatitis B Virus X Protein Function Requires Zinc Binding. *J. Virol.* **2019**, *93*, e00250−19.
(65) Amatya, P.; Wagner, N.; Chen, G.; Luthra, P.; Shi, L.; Borek, D.; Pavlenco, A.; Rohrs, H.; Basler, C. F.; Sidhu, S. S.; Gross, M. L.; Leung, D. W. Inhibition of Marburg Virus RNA Synthesis by a Synthetic Anti-VP35 Antibody. *ACS Infect. Dis.* **2019**, *5*, 1385−1396.
(66) Houde, D.; Berkowitz, S. A.; Engen, J. R. The Utility of Hydrogen/Deuterium Exchange Mass Spectrometry in Biopharmaceutical Comparability Studies. *J. Pharm. Sci.* **2011**, *100*, 2071−2086.
(67) Weis, D. D. Comment on Houde, D.; Berkowitz, S. A.; Engen, J. R., The Utility of Hydrogen/Deuterium Exchange Mass Spectrometry in Biopharmaceutical Comparability Studies. J. Pharm. Sci. 2011, 100, 2071-2086. *J. Pharm. Sci.* **2019**, *108*, 807−810.

https://doi.org/10.1021/acsinfecdis.1c00403
ACS Infect. Dis. 2022, 8, 118−128